Dynamic response and energy absorption of mineral–phenolic foam subjected to shock loading

Matteo Colombo [a], Paolo Martinelli [a,*], Roberto Zedda [b], Aldino Albertelli [b], Nicola Marino [c]

[a] *Department of Civil and Environmental Engineering, Politecnico di Milano, P.za L. da Vinci 32, 20133 Milano, Italy*
[b] *Acell Industries Ltd, 26 Upper Pembroke Street, Dublin 2, Ireland*
[c] *IDS Ingegneria Dei Sistemi, Via Enrica Calabresi 24, 56121 Pisa, Italy*

Received 19 January 2015
Revised 24 March 2015
Accepted 8 April 2015
Available online 9 April 2015

1. Introduction

Phenolic foam has received a great deal of attention in recent years thank to its excellent fire properties, including low flammability, low generation of toxic gas and no dripping during combustion [1–4]. Moreover, it is characterized by a low heat conduction coefficient, it is thermally stable over a broad temperature range [5,6] and is one of the less expensive foams compared to other polymeric foams available on the market. Because of its excellent fire properties, phenolic foam is gradually replacing other mar-ket-leading polymeric foams as polyvinyl chloride (PVC), polystyr-ene (PS), and polyurethane (PU) foams in fields where the requirements for flame, smoke and toxicity are stringent, such as building materials for civil construction, chemical industry, aero-space application and naval vessels [7,8]. However, the main draw-back of phenolic foam is its intrinsic brittleness that causes low strength and high friability and this has heavily limited its use in structural applications [2,9,10]. These drawbacks also lead to skin debonding in sandwich structures and dust pollution in the work-space. In recent decades, many attempts were undertaken to improve the toughness properties of phenolic foam, and these mainly fall into three categories [7]: chemical modification [11], inert fillers [9] and fibre reinforcement [12]. These last references are certainly not comprehensive but are only given as an example. This work refers to a particular type of foam that is defined as mineral–phenolic foam since it is characterized by a phenolic resin and a significant content of inert minerals.

If on the one hand this foam is used in a wide range of applications where high fire properties are required, on the other hand the advent of several blast attacks on civil, naval and defence structures requires a proper understanding of the blast response and resistance of the material. Dynamic properties of materials similar to that considered in this paper have never been, to the authors' knowledge, investigated so far. Nevertheless, the foam dynamic response as well as its energy absorption capacity is essential in order to develop new materials with enhanced blast resistance performance. For this reason, the aim of this study is to conduct a preliminary investigation, based on experimental tests and finite element (FE) numerical simulations, into the dynamic behaviour of mineral–phenolic foam. A simplified approach based on elasto-plastic single degree of freedom (SDOF) system is also proposed for the evaluation of the energy absorption capacity. The frame-work of this research is the application of mineral–phenolic foam prisms as energy absorbing elements when introduced in the external envelope of prefabricated modular shelters; these ele-ments are designed to resist a target explosion of 100 kg of equivalent TNT at a distance of 10 m. Future studies will be devoted to

* Corresponding author.
E-mail address: paolo.martinelli@polimi.it (P. Martinelli).

investigating the blast response of composite panels with mineral–phenolic foam core.

2. Material

The mineral–phenolic foam discussed in this paper is produced by Acell [13] and is a composite made with phenolic resin and variable quantities of inert minerals (gypsum, graphite, carbon, etc.). Compared to traditional phenolic foams it avoids their typical friability and has enhanced mechanical properties.

The production process does not use any blowing agents, as for instance CFC (chlorofluorocarbon), HCFC (hydrochlorofluorocarbons) or VOC (Volatile Organic Compound) and the result is a foam that can be recycled as powdered charges.

The foam considered has open cells with a controlled cell size. Nevertheless, a random cell size distribution characterizes the material differently from a honeycomb structure. The Acell production process allows the use of the same formulation to manufacture foams with different densities (from 80 to 800 kg/m^3), different cell sizes (from 0.2 mm to 5 mm) and therefore with different physical and mechanical properties. Table 1 reports the main physical properties of the foam considered in this study.

A view of the cell microstructure obtained with optical microscopy with an enlargement of 10, 30 and 100 times is shown in Fig. 1a–c, respectively. The material is characterized by an open-cell structure with an average cell size ranging between 0.5 and 1.5 mm, while the cell wall thickness ranges between 40 and 60 μm. The open-cell structure allows intercommunication between adjacent cavities and the air evacuation during the compression process.

This foam is generally used as the internal core of composite products with external SMC (Sheet Moulding Compound) layers. The Acell production process allows composite structures to be obtained with high performance (combining thermal insulation, fire resistance and structural properties) and an almost infinite range of finishes, without the fabrication steps normally required in the more conventional composite structures.

3. Uniaxial compressive behaviour

The mechanical behaviour of the mineral–phenolic foam in uniaxial compression is investigated at four strain rate (1×10^{-4}, 1×10^{-3}, 1×10^{-2} and $0.1\ s^{-1}$) from a quasi-static regime ($1 \times 10^{-4}\ s^{-1}$) to low/intermediate strain rates ($0.1\ s^{-1}$). The structural behaviour of the specimen under medium strain rate (up to $10^2\ s^{-1}$) is investigated through a shock tube apparatus as described in the following sections.

The material uniaxial behaviour is identified by means of tests on cubic specimens having a side length of 65 mm. The tests are carried out by means of an electromechanical press (Instron 5867) with a bearing capacity of 30 kN and a precision equal to 0.4%; the stroke is considered as feedback parameter. The specimens are placed between two steel press plates (Fig. 2a); in order to reduce friction, on the specimen faces in contact with the plates, stearic acid is applied [14].

Table 1
Properties of the Acell mineral–phenolic foam.

Property		Standard	Value
Density[§]	(kg/m^3)	–	120
Thermal conductivity	(kcal/m h °C)	UNI 7745	0.037
Linear coefficient of thermal expansion	(m/m °C $\times 10^{-6}$)	BS 4371 p.3	20/40
Moisture properties	(–)	DIN 52615	70
Smoke generation and toxic gas emission	(Aeronautical railway)	ATS 1000.001 NF F 16-101	Passed M1 F1
Punking	(–)	BS 5946	Passed

[§] ±10%.

For each strain rate considered, three nominally identical tests are carried out giving a total of 4×3 tests. The average nominal stress–strain behaviour computed on three identical specimens is shown in Fig. 2b for the four strain rates considered. The material shows a strain rate insensitivity in the strain rate range considered.

From the average experimental stress–strain curves, an elasto-perfectly plastic constitutive law is derived; it is described by the following equation:

$$\sigma_N = \begin{cases} (27 \times 10^6)\varepsilon_N \\ 0.40 \times 10^6 \end{cases} \quad \text{if} \quad \begin{cases} \varepsilon_N < 1.481 \times 10^{-2} \\ \varepsilon_N > 1.481 \times 10^{-2} \end{cases} [\text{Pa}] \tag{1}$$

The elastic region is characterized by a Young's modulus of 27 MPa, while the compressive yield strength is about 0.40 MPa. In Fig. 3a it is interesting to observe how the yield strength (σ_y) and the Young's modulus (E) values remain almost constant vary-ing the strain rate in the low/intermediate values range. Similar considerations can be extended to the plastic energy dissipation, E_P, that is not affected by the strain rate (Fig. 3b). The specific plas-tic energy dissipation, also referred as specific energy absorption (SEA), of the material at strain values of 0.1 and 0.2 is equal to about 35 kJ/m^3 and 75 kJ/m^3, respectively.

The post-test inspection of the specimens under the microscope revealed that during the compression phase the progressive collapse of internal cell wall gradually provides intercommunication between adjacent pores, leading ultimately to a nearly full void interconnection. This experimental evidence is confirmed by the fact that, if the specimen is unloaded from any stage of the compression test, the material does not show any appreciable elastic return which would be caused by the relaxation of the air pressure. This phenomenon was also pointed out by [15].

4. Shock tube tests

4.1. Shock tube equipment

The shock wave tests are carried out in the Shock Tube Laboratory of Politecnico di Milano. The present double diaphragm shock tube facility is used as blast simulator; the use of shock tubes to simulate blast loading on structures is not new and this technique was developed to reproduce blast waves nearly identical to those obtained in live explosive tests [16,17]. The shock tube facility was recently adopted to investigate the behaviour of underground tunnel linings under blast conditions [18,19]. The shock tube adopted in this study is able to produce a high-pressure loading range, with a maximum reflected target pressure of about 3 MPa. It can be distinguished from other shock tubes by a suitable end chamber designed to investigate soil-structure interaction and by an appropriate burner equipment to heat specimen intrados according to a defined fire curve. Both these peculiarities are not used in present work. A detailed description of all the shock tube components can be found in [20]; only the main points of interest are summarized below.

A schematic layout of the shock tube device in the assembled configuration is shown in Fig. 4a. It consists of three chambers that can move on a linear guide system: the driver chamber, the buffer or diaphragm chamber and the driven chamber. The test area is placed at the end of the driven chamber. The total shock tube length excluding the test area is 13.11 m. The tests are carried out using pressurized helium inside the driver and buffer cham-bers, and air at ambient condition in the driven chamber.

Driver, buffer and driven chambers have a length of 2.35, 0.26 and 10.5 m, respectively, with an internal diameter of 481 mm. The driver and driven chambers have a 13.5 mm thick wall, while

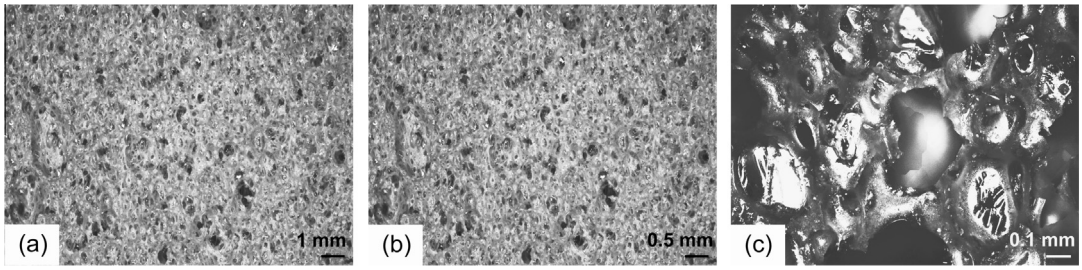

Fig. 1. Cell microstructure of the mineral–phenolic foam: (a) 10×, (b) 30× and (c) 100×.

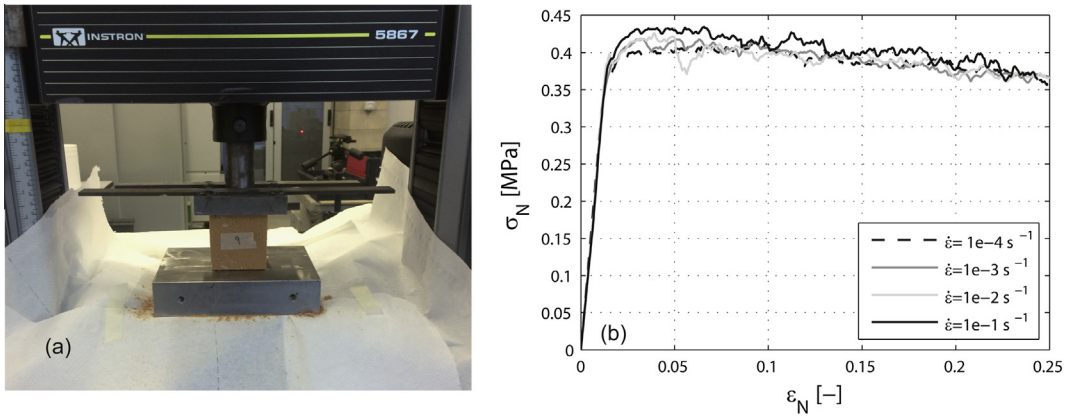

Fig. 2. Uniaxial compressive tests on mineral–phenolic foam specimens: (a) test set-up and (b) nominal stress–strain curves ($\sigma_N = P/A$; $\varepsilon_N = \delta/L$; σ_N = nominal stress; ε_N = nominal strain; P = applied load; A = cross-section area; δ = axial displacement; L = initial height).

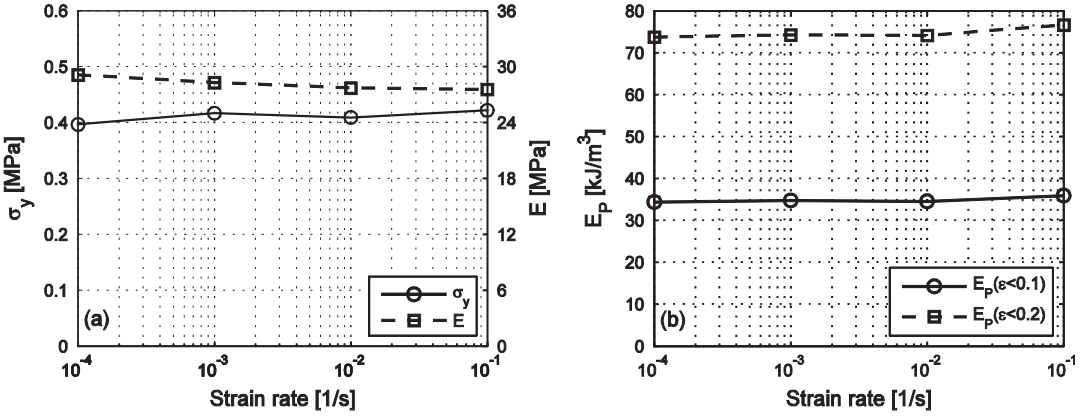

Fig. 3. (a) Yield strength and Young's modulus values at different strain rate and (b) specific plastic energy dissipated at different strain rate for strains lower than 0.1 and 0.2.

the buffer chamber has an external diameter of 857 mm that corresponds to the maximum diameter of the flange welded on the driver and driven ends.

When the two scored steel diaphragms that separate the buffer chamber from the driver and driven chambers fail and form four petals, the rapid propagation of the pressurized gas into the driven chamber occurs and leads to the creation of a shock wave. It is worth noting that no breaking devices are used to force the opening of the diaphragms, but the diaphragms' failure is obtained by a differential pressure created between the driver/buffer and buffer/-driven chambers. Further details on the firing mechanism can be found in [20].

4.2. Test set-up

This section describes the test set-up designed to conduct the experimental tests. The test equipment consists of a circular steel plate load diffuser, a steel reaction flange, 20 steel cylindrical spacers and two prismatic mineral–phenolic foam specimens (see Fig. 4b). The choice of two nominally identical specimens instead of one is aimed to reproduce the structural application in the prefabricated shelters that involves the use of pairs of mineral–phenolic prisms as supports of composite panels where the supports represent the main source of dissipation in the case of blast loads. The testing method reliability is proved in Appendix A.

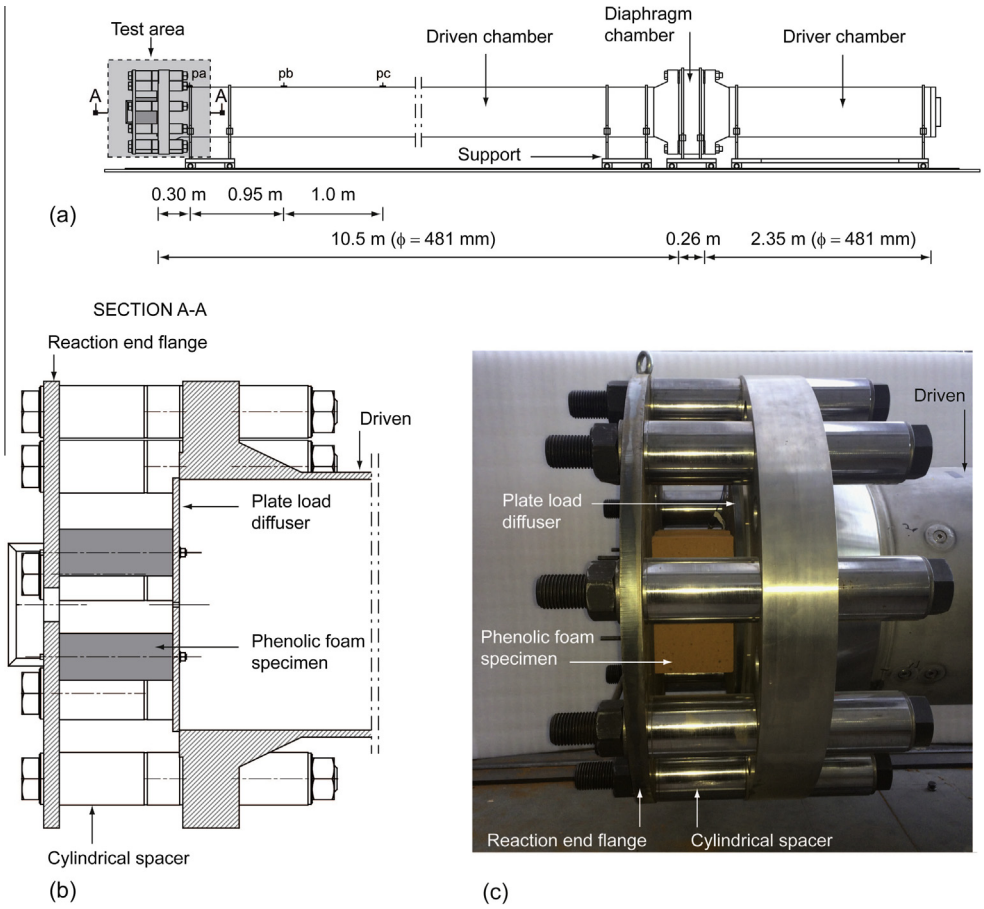

Fig. 4. (a) Lateral view of the shock tube facility, (b) horizontal section of the test set-up area and (c) picture of the test set-up.

The reaction end flange is connected to the driven end flange through ten M52 bolts. The foam specimens are glued onto the internal side of the reaction end flange. The cylindrical spacers are inserted to allow the positioning of the foam specimens between the reaction flange and the driven end. The circular load diffuser can move along the tube axial direction driven by a sleeve system made by four M10 screws connected to the reaction flange passing through four corresponding holes placed in the diffuser. Once the shock wave reaches the driven end, it strikes the plate dif-fuser that uniformly compresses the two prismatic foam specimens.

The cylindrical spacers have an external diameter of 101 mm and an internal hole diameter of 54 mm that allows the insertion of the M52 screws. The spacers have different lengths depending on foam size. The plate diffuser has a diameter of 485 mm and a thickness of 12.5 mm. On the plate diffuser several instruments are mounted as discussed in the next section. The reaction flange has the same diameter of the driven end flange (857.2 mm) and a thickness of 30 mm. It has been machined in order to have holes of the same dimension (54 mm) and half the number (ten) of the bolt holes of the driven flange: this permits the reaction flange to be bolted together with the driven chamber. A picture of the test set-up area is shown in Fig. 4c.

4.3. Specimen sizes, instrumentations and test programme

The mineral–phenolic foam specimens have a prismatic shape, the sizes of which are detailed in Fig. 5a. Previous studies (see for example [21]) on other open-cell foams, show that no size effect is observed if the minimum specimen dimension is larger than 12 times the cell size. Assuming this result also valid for the material investigated, no size effect is expected because the aforementioned condition is satisfied. In each test, two identical specimens are used in parallel as indicated in Fig. 5b and c. The specimens are glued onto the reaction flange and are in contact with the plate diffuser. The position of the foam specimens on the plate load diffuser is also given in Fig. 5b and c.

The behaviour of the mineral–phenolic foam specimens is investigated through an appropriate set of instruments, in part positioned on the driven chamber and in part positioned on the plate diffuser.

Three ICP (Integrate Circuit Piezoelectric) dynamic pressure transducers indicated as pa, pb and pc are placed along the driven chamber axis at 300 mm (pa), 1250 mm (pb) and 2250 mm (pc) from its flange end (Fig. 4a). Other two dynamic pressure transducers (indicated as p1 and p2 in the following) are mounted directly onto the circular plate diffuser: p1 is placed at the plate centre while p2 is placed at 200 mm from the plate centre along the vertical direction (Fig. 5c–d). The transducers p1 and p2 allow the load applied on the specimens to be obtained directly. The transducers have a quartz sensing element with a full-scale pressure of 6.9 MPa, a sensitivity of 0.7 mV/kPa, a rise time lower than 1 μs and a resonant frequency higher than 500 kHz.

The plate diffuser acceleration is measured by means of one ICP accelerometer (A1) placed at the plate centre and measuring the acceleration along the tube axis. The accelerometer characteristics are a quartz sensing element with a measuring range of ±500 g pk (peak acceleration), a band width larger than 10 kHz, a broadband resolution of 0.005 g rms (root mean square) and a resonant frequency higher than 70 kHz. The accelerometer A1 indirectly allows

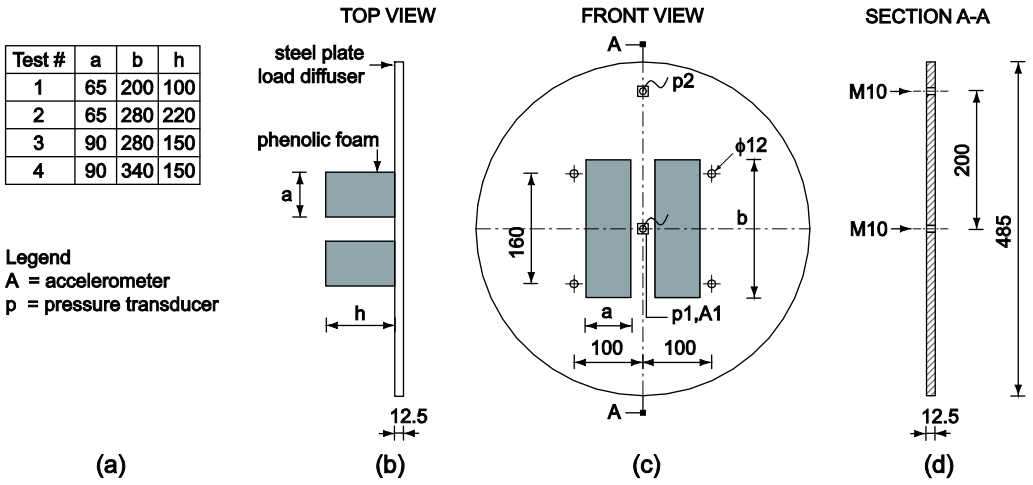

Fig. 5. Specimen dimensions and location of the instruments: (a) specimen sizes, (b) top view, (c) front view and (d) plate diffuser vertical section (units: mm).

the diffuser plate velocity and displacement to be obtained by single and double integration, respectively, as will be described in Section 7.

In order to validate the indirect displacement measure obtained by double integration, a direct measure of the plate diffuser displacement is recorded by using a high-speed camera placed orthogonally to the shock tube axis. The high-speed camera has a resolution of 256 × 256 pixels, a sample rate of 13,029 samples/s (13 kS/s) and an exposure time of 20 ms. The high-speed camera equipment is only used for the Test4.

The signal conditioning for both accelerometer and pressure transducers is performed with an ICP signal conditioner with gain equal to one, a bandwidth equal to 10 kHz and a broadband electrical noise equal to 3.5 μV rms.

All channels are acquired by means of the same data acquisition system with 56 parallel channels with the maximum sampling rate of 3 MS/s per channel and a 14-bit resolution. The data acquisition for all the channels is triggered by the signal of the pressure transducer (pc) placed at a distance of 2250 mm from the driven end flange: when the shock wave goes through its position, the system starts acquiring data with a sampling rate of 1 MS/s.

A total of four tests are carried out with the same nominal load history. The tests differ for the different sizes of the foam specimens as indicated in Fig. 5a. The tests are characterized by an average peak pressure of 0.46 MPa and an average specific impulse of 2.57 MPa ms. A progressive numerical number is used to indicate different tests that correspond to different specimens (Test1, Test2, Test3, and Test4).

5. Finite element model

The FE model, developed using the commercial code Abaqus/Explicit 6.12 [22], is used to simulate the dynamic response of mineral–phenolic foam specimens. The model includes the reaction end flange, the plate diffuser and the two prismatic foam specimens.

Eight-node reduced integration and hourglass control brick elements (C3D8R) with three degrees of freedom per node are employed to discretise the foam specimens. Three-node triangular shell elements with reduced integration, hourglass control and a large strain formulation (S3R) are adopted to discretize the reaction end flange and the plate diffuser. The shell element has one integration point over the reference plane and six degrees of freedom per node; five integration points are used along the thickness. The reaction end flange is idealized as fully fixed along its external

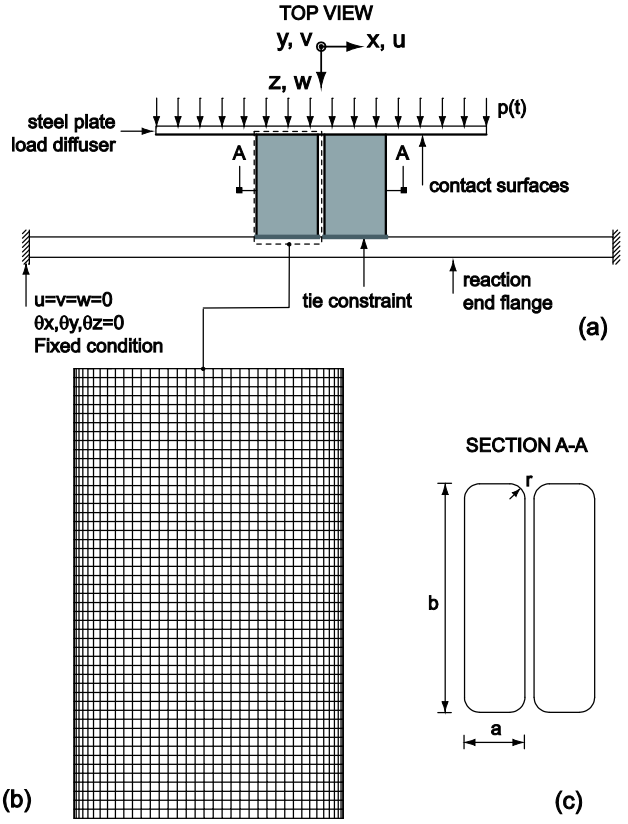

Fig. 6. (a) Boundary conditions, load and interaction surfaces of the FE model, (b) top view mesh for a single mineral–phenolic foam specimen (Test4) and (c) detail of the rounded corners.

circumference; the foam specimens are connected, along the *z*-direction to the reaction end flange through tie elements (Fig. 6a). The contact interaction between the plate diffuser and the foam specimens is modelled by the contact pair algorithm provided by the ABAQUS package [22]. A "hard contact" is used in normal direc-tion while the classical friction model based on Coulomb approx-imation (friction coefficient μ = 0.1) is used to simulate the tangential interaction between the plate diffuser and the foam specimens' surfaces (Fig. 4a). The two dynamic pressure transducers p1 and p2 applied on the plate diffuser allow the load applied on it

to be obtained directly. The load applied in the numerical analyses is the average between the experimental signals p1 and p2.

The boundary conditions, the load applied and the interaction surfaces (tie elements and contact surfaces) are detailed in Fig. 6a. The FE mesh used to model the prismatic mineral–phenolic foam specimen for Test4 is shown in Fig. 6b (Test4: total node number equal to 450,824, total element number equal to 431,421, total linear brick element number 424,800, total triangular shell element number 6621).

The 90 degrees angles between edges a and b are slightly rounded (radius r = 22.5 mm) to limit the distortion of the elements that may occur at the singularity points of the foam specimens during the contact process with the plate diffuser (Fig. 6c).

A linear elastic material is assumed for the reaction end flange and the plate diffuser, both made of steel (Young's modulus E = 210 GPa, Poisson's ratio v = 0.3 and density ρ = 7850 kg/m^3).

The mineral–phenolic foam is modelled by a crushable foam plasticity model with volumetric hardening [23]. The elastic part of the foam response is characterized by a Young's modulus E = 27 MPa and Poisson's ratio v = 0.1. For the plastic part, the crushable foam model assumes an elliptical yield surface in devia-toric stress and hydrostatic stress plane. The model requires two parameters (k and k_t): k is the compression yield stress ratio defined as the ratio of initial yield stress in uniaxial compression to initial yield stress in hydrostatic compression, while k_t is the hydrostatic yield stress ratio defined as the ratio of strength in hydrostatic tension to initial yield stress in hydrostatic compression.

Nominal stresses and strains obtained from the experimental uniaxial compression tests described in Section 3 are then converted into true stresses and logarithmic plastic strains which are used as input data in the numerical FE simulations. The hardening behaviour is defined in terms of uniaxial compressive yield stress σ_c and uniaxial compressive plastic strain ε^{pl}_{axial}. Uniaxial logarithmic plastic strain is obtained from nominal engineering strain as:

$$\varepsilon^{pl}_{axial} = \ln(1+\varepsilon_{nom}) - \varepsilon^{el} \tag{2}$$

where ε_{nom} is the nominal engineering strain and ε^{el} is the elastic strain.

In modelling the dynamic foam behaviour, the hypothesis of strain rate independent properties is assumed. The comparison between experimental and numerical results discussed in Section 7 will prove the validity of this hypothesis up to a maximum strain rate $\dot{\varepsilon}$ of about 100 s^{-1} (value reached during the experimental tests). The mechanical properties of the mineral–phenolic foam used in the FE model are given in Table 2.

6. Single degree of freedom model

A simplified discrete mass-spring model is created to study qualitatively the mineral–phenolic specimen response (displacement history) and its energy absorbing capacity. This model consists of an equivalent elasto-perfectly plastic single degree of freedom (SDOF) system. For the particular experimental set-up adopted (see Fig. 4), it is not necessary to resort to the use of principle of virtual displacement in the determination of coefficients that relate the equivalent mass, stiffness and load in the SDOF system to their respective quantities in the actual system. In particular, the mass m of the SDOF system is given by the mass of the steel plate diffuser that is much larger than the mass of the foam specimens. On the other hand, the total stiffness K of the SDOF system is obtained as $K = 2 \times k_f$, where k_f is the axial stiffness of the single mineral–phenolic foam specimen; the two foam specimens are in fact working as a parallel springs system. The stiffness k_f is directly extrapolated by the constitutive law indicated in Eq. (1). The load applied on the SDOF system is derived from the average experimental pressures measured by transducers p1 and p2 multiplied by the area of the plate diffuser.

The following numerical values are assumed in the analysis and completely describe the elasto-plastic SDOF system: m = 17.75 kg, $K = 11.02 \times 10^6$ N/m and $\delta_y = 2.221 \times 10^{-3}$ m, where δ_y is the yield displacement.

Table 2
Mechanical properties of mineral–phenolic foam.

Density (kg/m^3)	ρ = 120
Young's modulus (MPa)	E = 27
Poisson's ratio (–)	v = 0.1
Initial uniaxial compressive yield stress (MPa)	σ_{c0} = 0.40
Compression yield stress ratio (–)	k = 1.0
Hydrostatic yield stress ratio (–)	k_t = 0.1

7. Results and discussion

The present section describes the results obtained in the experimental investigation and compares them with the numerical and analytical predictions given by FE and SDOF models.

The pressure histories recorded during each test are presented in Fig. 7 where the measurements of the pressure transducers flush mounted on the plate diffuser surface (p1 and p2) are compared with that of transducer placed on the shock tube wall at 300 mm from the specimen position (pa). Unfortunately, electric problems arose during the tests, causing the loss of both pressure signals p1 and p2 for Test1 and of pressure transducer pa during Test4.

The comparison between signals p1 and p2 indicates that the pressure distribution along the diffuser plate is almost constant thus confirming the planarity of the shock waves impinging the specimens.

Looking at the pressure signals directly recorded on the plate diffuser (Fig. 7), it is possible to observe the sudden pressure rise due to the reflection of the shock wave over the plate when the incident shock wave reaches the specimen. In order to better compare all the tests, the time in which this sudden pressure increment occurs is considered as the initial reference time (t = 0) for all the measurements of the same test. This means that negative time values in the following figures refer to instants in which the specimen is not yet loaded by the shock wave.

Pressure measurements recorded on the tube wall surface clearly show the two different contributions of the incident wave travelling in the tube (first rise at about $t = -1$ ms) and of the subsequent reflected wave travelling back from the specimen (second rise at about t = 1 ms). The attenuation of the reflected wave pressure travelling back in the driven chamber can be also observed comparing the pressure peak reduction between pressures measured on the plate diffuser and in the driven chamber.

In Fig. 8 the average curves between pressure signals p1 and p2 for each test are compared thus showing the good repeatability of the applied pressure histories in all the tests.

The central accelerations of the plate diffuser are compared in Fig. 9a for all the experimental tests. Because of the different geometry of the specimens considered in each test it is not possible to define a unique trend even if the maximum acceleration recorded is of the same order of magnitude for all the situations investigated. The maximum peak accelerations range between 0.636×10^4 m/s^2 (Test2) and 1.015×10^4 m/s^2 (Test1).

A double time integration procedure is applied to the acceleration signal in order to compute respectively the plate velocity (first integration) and the plate displacement (second integration). The reliability of this procedure is assessed in Fig. 9b where, for the case of Test4, the displacement computed according to this

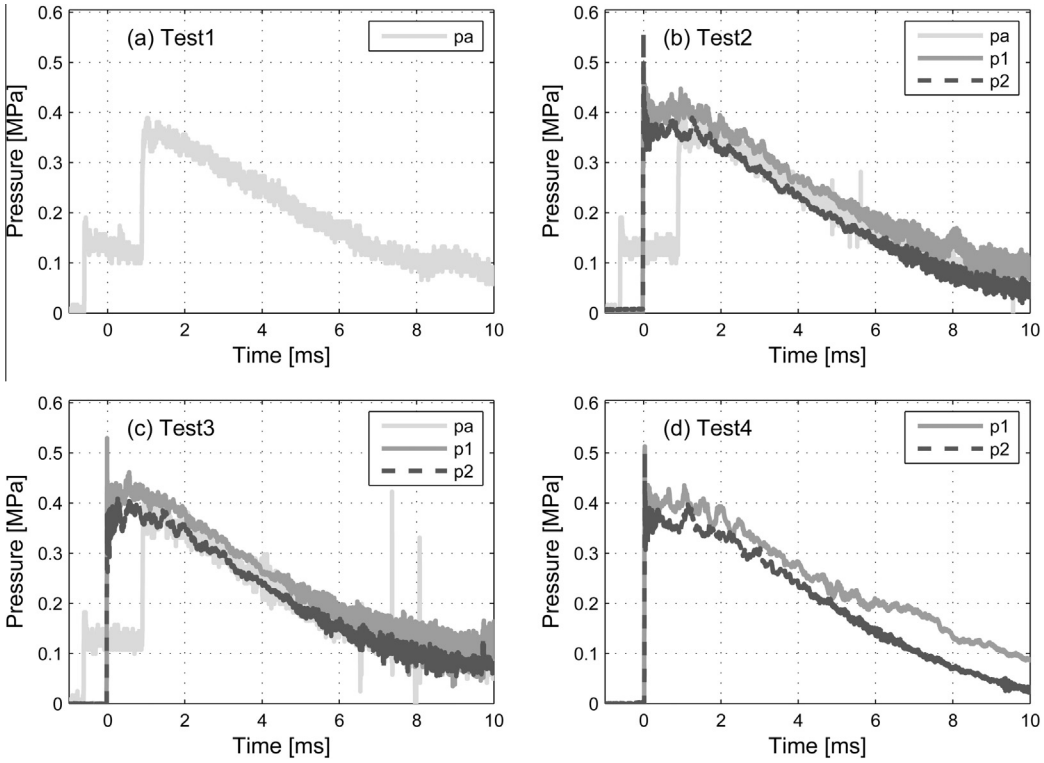

Fig. 7. Pressure histories recorded at the end of the shock tube driven chamber (pa) and on the plate diffuser (p1 and p2) for (a–d) Test1–Test4.

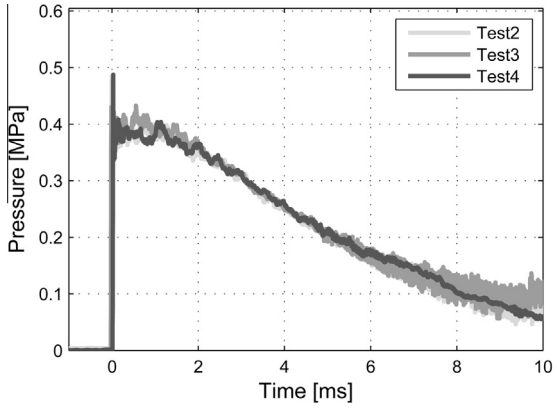

Fig. 8. Average pressure time histories (mean of pressure transducers p1 and p2) recorded on the plate diffuser during the experimental tests.

procedure (“accel. integration”) is compared with the plate displacement measured by means of digital image processing of the high-speed video recorded during the test (“measured”).

It is worth noting that after reaching the maximum displacement, the plate diffuser starts moving backwards detaching from the mineral–phenolic foam specimens, thus causing the descending branch visible in Fig. 9b. Taking advantage of this consideration, it is important to emphasize that the displacement of the plate is representative of the compression behaviour of the foam only until the peak of the displacement response, that corresponds to the instant when the separation between the plate and the specimen takes place.

Once the reliability of the time integration procedure is assessed, plate diffuser velocity and displacement are computed for each test and a comparison is presented in Fig. 10, where both velocity and displacement are normalized with respect to the initial specimen length (L). The different dimensions of the specimens (not only in length but also in cross-section) is the main reason for the different structural responses when exposed to a very similar load history. The maximum strain rate ($(\partial\delta/\partial t)/L$) ranges between 50 and 100 s^{-1} (Fig. 10a), while the maximum axial strain (δ/L) ranges between 70% and 85% (Fig. 10b).

The prediction capability of FE and SDOF models is presented here by considering Test4 as a reference case. As already discussed, both numerical and analytical models consider an applied pressure history equal to the experimental average between pressure signals p1 and p2. The results of the models are shown in Fig. 11 in terms of plate displacement (δ) time history; in the same figure, a comparison with the experimental results shows the good reliability of the models.

Both FE and SDOF models reproduce the material non-linear behaviour for very large deformation values in a satisfactory way, even if the FE approach provides a more precise prediction especially in the final part of the specimen response (t > 10 ms). The more complete kinematic, the 3D constitutive model as well as the geometrical nonlinearities justify the better prediction of FE model.

It is worth noting that both approaches do not consider any strain rate dependency in the constitutive relationship. This consideration, backed up by the experimental results, may lead to conclude that the mineral–phenolic foam examined is almost strain rate independent in the range of strain rate considered.

The FE model results are also compared with the experimental ones in Fig. 12, where the deformed shapes representing the minimum principal plastic strain contour are compared with the images of the experimental test at different time steps.

When considering crushable material for blast load mitigation, energy absorption capacity is a very important issue. In order to compute the absorption capacity of this material some considerations can be made once again focusing on the FE model results (Test4).

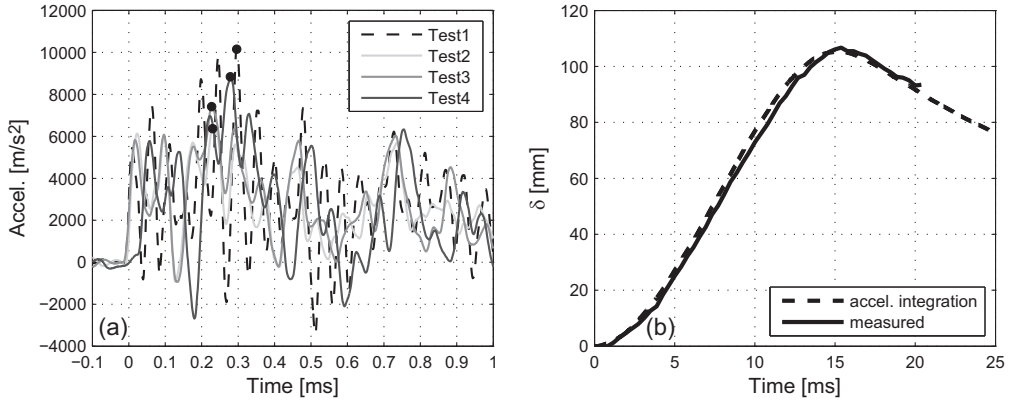

Fig. 9. (a) Axial central plate acceleration recorded during the experimental tests and (b) direct ("measured") and indirect ("accel. Integration") displacement response for Test4.

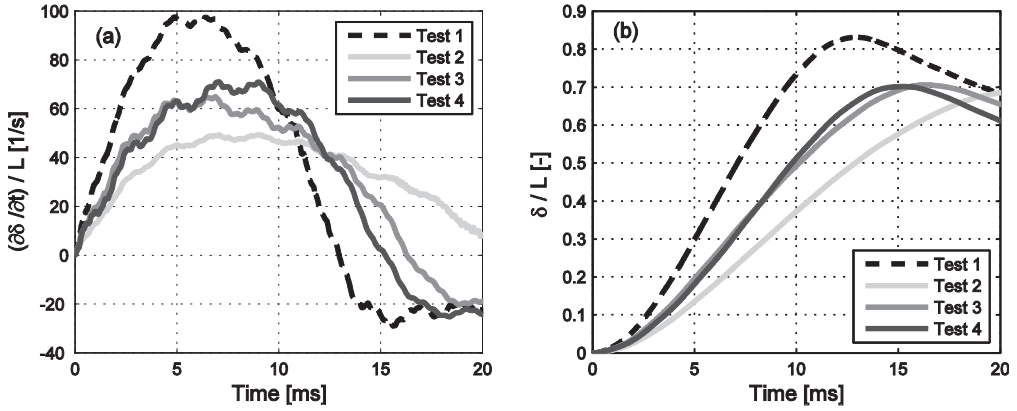

Fig. 10. Normalized experimental responses: (a) velocity and (b) displacement for the four experimental tests.

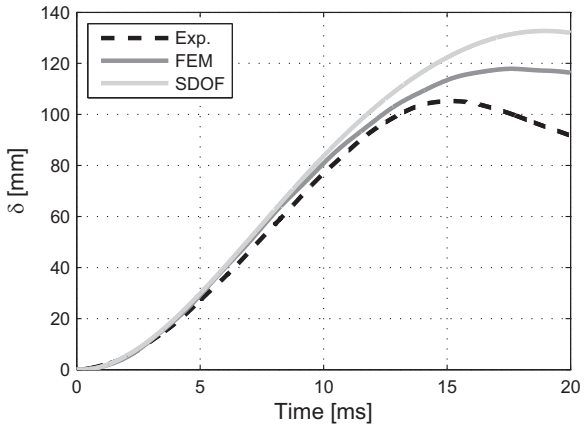

Fig. 11. Displacement response comparison between experimental data, FE analysis and SDOF system (Test4).

The following energy balance is assumed for the model:

$$E_I + E_{KE} - E_W = E_{tot} = const \tag{3}$$

where E_I is the internal energy, E_{KE} is the kinetic energy and E_W is the work done by the externally applied loads. The sum of these energy components is E_{tot}, which should be constant.

It is assumed that the internal energy E_I is the sum of the recoverable elastic strain energy E_E and the energy dissipated through plasticity E_P:

$$E_I = E_E + E_P \tag{4}$$

In Eq. (4) the strain energy E_E is small in comparison with E_P (less than 1.5% of E_P) and is neglected. Eq. (4) can be written as:

$$E_I \cong E_P \tag{5}$$

Substituting Eq. (5) in Eq. (3), this last can be rewritten as:

$$E_P + E_{KE} - E_W = E_{tot} = 0 \tag{6}$$

From Eq. (6) it is possible to calculate an estimation of the plastic energy:

$$E_P^* = E_W - E_{KE} \tag{7}$$

where E_P^* is the estimated plastic energy.

Fig. 13a shows the time histories of different energies involved in the deformation process (E_W, E_{KE}, E_P and E_E) directly recorded by the FE model. Looking at the results, it is clear that the material dissipates a huge amount of the external work by means of plastic dissipation and confirms that E_E is negligible.

Plastic dissipation can also be evaluated for the SDOF model at each time t as the integral of the load vs plastic displacement (generalized constitutive relationship) in the interval between zero and the maximum plastic displacement achieved by the system between zero and t. The evolution of the SDOF plastic dissipation ("SDOF E_P") is represented in Fig. 13b; in the same figure, the plastic dissipation energy obtained by the numerical FE analysis ("FEM E_P") is also reported.

In Fig. 13b two other curves ("FEM E_P^*" and "EXP E_P^*") are reported: they represent an estimation of plastic dissipation

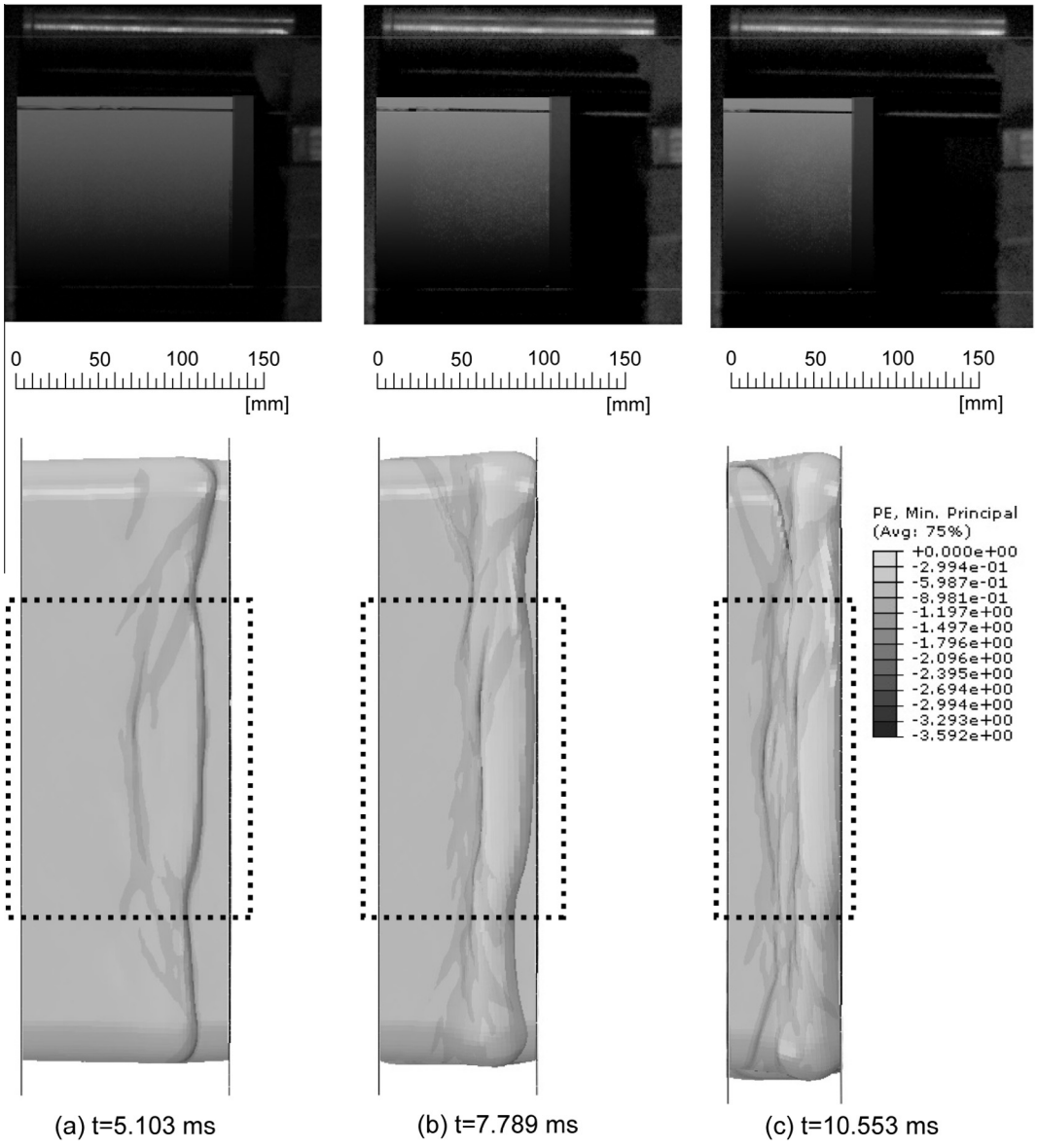

Fig. 12. High-speed images for Test4 and corresponding FE minimum principal plastic strains at several time steps: (a) t = 5.103 ms, (b) t = 7.789 ms and (c) t = 10.553 ms.

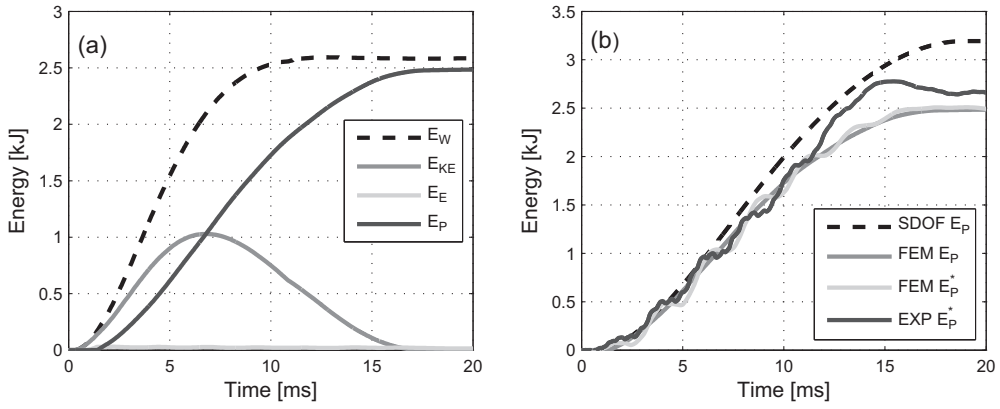

Fig. 13. (a) Numerical FE energies computed for Test4 and (b) plastic dissipation energy comparison between experimental data and numerical (FE and SDOF) results (E_W = external work; E_{KE} = kinetic energy; E_E = strain energy; E_P = plastic energy).

Table 3
Comparison of specific energy absorption of mineral–phenolic foam with those of other types of polymeric foams.

Material	Density (kg/m^3)	Strain rate (s^{-1})	Specific energy absorption (kJ/m^3)	Reference
Mineral–phenolic foam	120	70	299	This paper
EPS foam	13.5	0.001–65–185	224–301–319	[24]
EPS foam	28.0	0.001–65–185	404–497–497	[24]
EPS foam	12.8	0.00833–0.04167–0.08333	105–119–135	[25]
EPS foam	55	Quasi-static	250	[26]
EPS foam	70	Quasi-static	380	[26]
PVC foam	40–80–130–200	Quasi-static	360–1123–1975–3300	[27]
PVC foam	75	0.001–0.01–0.1–700–1000–1600	102–102–102–154–154–102	[28]
PVC foam	130	0.001–0.01–0.1–700–1200–1600	307–307–358–307–307–410	[28]
PVC foam	300	0.001–0.01–0.1–700–1200–1600	922–1024–1075–1894–1843–1946	[28]
PU foam	320	0.001–0.01–0.1–700–1200–1600	870–870–1024–922–1024–819	[28]
PU foam	246	0.01–700–1200–1600	256–358–409–460	[28]

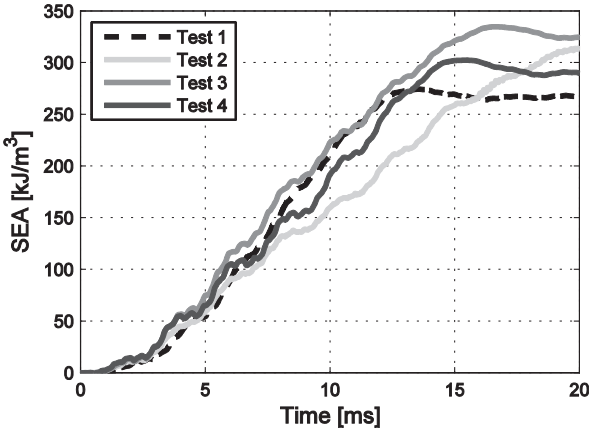

Fig. 14. Specific energy absorption (SEA) computed during the experimental tests.

energy computed applying Eq. (7). The measurements of the applied pressure history ($p(t)$), of the plate displacement ($\delta(t)$) and velocity ($v(t)$) at each time t allow to calculate E_W and E_{KE}.

The external work E_W made by the pressure $p(t)$ at a certain time t can be computed as:

$$E_W(t) = \int_0^t p(t) \cdot \delta(t) \cdot dt \tag{8}$$

The kinetic energy E_{KE} of the system at a certain time t, neglecting the mass of the foam and just considering the mass of the steel plate diffuser m, is given by:

$$E_{KE}(t) = \frac{1}{2} m \cdot v(t)^2 \tag{9}$$

In Fig. 13b, the curve "FEM E_P^*" is calculated by applying Eqs.(7)–(9) and using pressure, displacement and velocity obtained from the FE model while "EXP E_P^*" applies the same equations by using pressure, displacement and velocity obtained from the experimental Test4, the evolutions of which are already shown respectively in Figs. 8, 10a and b. In the same figure, the curve "FEM E_P" is the plastic energy directly recorded by the FE model.

The direct comparison in Fig. 13b between the curves "FEM E_P" and "FEM E_P^*" proves how Eq. (7) represents a reliable estimation of the dissipated energy highlighting that all other possible sources of dissipation play a negligible role. Eq. (7) can be applied to all the experimental test results to estimate the specific (per unit volume) plastic energy dissipation. In the case of Test1, where the pressure signals on the plate diffuser were lost, the external work is computed by using the pressure history of Test2; this assumption is allowed by the good repeatability of the pressure signals measured in all the tests performed (see Fig. 8). The specific energy dissipation evolution for all the tests is reported in Fig. 14, where a good repeatability of the energy dissipation response can be observed for all the specimens tested. This repeatability also confirms the assumption that no size effect affects the specimen geometries considered. The figure points out the good energy absorption capacity of the material investigated, characterized by a specific plastic dissipation energy of about 300 kJ/m^3.

Table 3 reports the average specific energy absorption of the four dynamic tests compared with the published data [24–28] on various polymeric foams (EPS, PVC and PU). An examination of Table 3 shows that the specific energy absorption value of the mineral–phenolic foam is similar than those measured on EPS, PVC and PU foam with similar densities. High density PVC and PU foams (200–320 kg/m^3) show specific energy absorption values higher than that measured on the material at study.

8. Conclusions

This paper reports the main findings of an experimental and numerical study focusing on the dynamic response at low-medium strain rate of mineral–phenolic foam. Moreover, the work explores the capability of mineral–phenolic foam to dissipate energy when subjected to shock loading.

Two experimental campaigns are carried out: the first one studies the uniaxial compressive behaviour at low strain rate (1×10^{-4}–1×10^{-1} s^{-1}); in the second campaign the experimental tests are conducted with an existing shock tube equipment through an ad-hoc modification of the test set-up area allowing to reach medium strain rate (50–100 s^{-1}).

The design of the shock tube set-up allows well-controlled pressure load histories to be applied to the specimens (high test repeatability). The load histories are characterized by a maximum pressure value of about 0.46 MPa and a positive phase duration of about 20 ms. Starting from direct measurements of acceleration, it has been possible to quantify, by single and double integration, the maximum strain rate and the maximum axial global strain.

The experimental investigation has shown the strain rate insensitivity of the material in the range considered. In addition, the tests have pointed out the good energy absorption capacity of the material investigated, if compared with other polymeric foams, characterized by a specific plastic dissipation energy of about 300 kJ/m^3.

Explicit finite element analyses have shown the adequacy of the crushable foam material model of ABAQUS in reproducing the compressive mineral–phenolic foam dynamic response. A simplified approach based on elasto-plastic single degree of freedom system provides a satisfactory estimation of the material energy

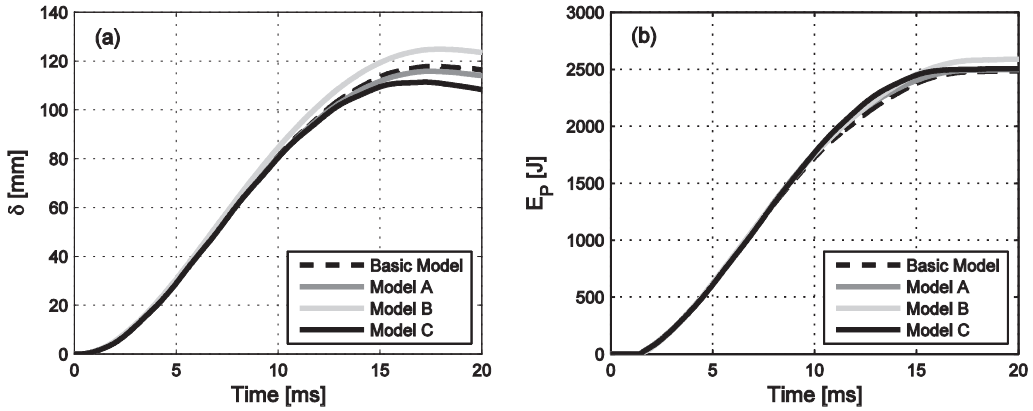

Fig. A1. Responses for the four FE models during Test4: (a) displacement and (b) plastic energy evolutions.

absorption capacity and of the global compressive dynamic response.

Acknowledgments

The authors want to thank Zenan Yan and Jie Zhang for their help in FE model simulations as a part of their M.Sc. thesis in Civil Engineering at Politecnico di Milano.

Appendix A

The use of two different specimens working in parallel, as already discussed, is strictly related to the structural application of the material. Nevertheless, the reliability of the test set-up has been assessed by means of a FE numerical investigation aimed at studying the main source of non-symmetry that may arise in the case of a double specimen set-up.

First of all, the variability of the mechanical properties of the materials of the two prisms has been investigated considering the two blocks made of two different materials (Model A) with Young's modulus and yield strength respectively +5% and −5% of the average values presented in Sections 3 and 6.

The possible different length of the two specimens has been taken into account by means of Model B in which one of the prism is kept to its original length (150 mm), while the other one is 2 mm shorter (148 mm), thus causing a non-contemporary contact of the diffuser plate with the two samples.

Finally, the influence of the double specimen set-up is also investigated by modelling, for comparison, a single specimen (Model C) characterized by the same global cross-section area of the two specimens.

The results of the models are reported in Fig. A1. In this figure the results are compared with the Basic model, discussed in Sections 5 and 7, in terms of displacement (Fig. A1a) and plastic dissipation (Fig. A1b) time histories. No significant differences are observable in the dissipated energy for all the situations investigated. Looking at the displacements, very similar responses are observable up to 15 ms, while the differences visible in the last part of the time histories are smaller than 7%.

References

[1] S. Lei, Q. Guo, D. Zhang, J. Shi, L. Liu, X. Wei, Preparation and properties of the phenolic foams with controllable nanometer pore structure, J. Appl. Polym. Sci. 117 (2010) 3545–3550.
[2] H. Shen, A.J. Lavoie, S.R. Nutt, Enhanced peel resistance of fiber reinforced phenolic foams, Compos. Part A-Appl. Sci. Manuf. 34 (2003) 941–948.
[3] H. Shen, S. Nutt, Mechanical characterization of short fiber reinforced phenolic foam, Compos. Part A-Appl. Sci. Manuf. 34 (2003) 899–906.
[4] A. Desai, M.L. Auad, H.B. Shen, S.R. Nutt, Mechanical behavior of hybrid composite phenolic foam, J. Cell. Plast. 44 (2008) 15–36.
[5] A.M. Papadopoulos, State of the art in thermal insulation materials and aims for future developments, Energy Build. 37 (2005) 77–86.
[6] A.H. Landrock, Handbook of Plastic Foams: Types, Properties, Manufacture, and Applications, vol. 2, 1995, p. 183.
[7] M.L. Auad, L. Zhao, H. Shen, S.R. Nutt, U. Sorathia, Flammability properties and mechanical performance of epoxy modified phenolic foams, J. Appl. Polym. Sci. 104 (2007) 1399–1407.
[8] L.Y. Wang, G.Q. Gai, H.Y. Yu, W.L. Liu, Preparation and performance investigation of phenolic foam, Adv. Mater. Res. 415–417 (2012) 1508–1511.
[9] V.K. Rangari, T.A. Hassan, Y. Zhou, H. Mahfuz, S. Jeelam, B.C. Prorok, Cloisite clay – infused phenolic foam nanocomposites, J. Appl. Polym. Sci. 103 (2007) 308–314.
[10] A. Desai, Fiber Reinforced Hybrid Phenolic Foam, Ph.D. Thesis, University of Southern California, Los Angeles, 2008.
[11] G. De Carvalho, E. Frollini, Lignin in phenolic closed cell foams: thermal stability and apparent density, J. Macromol. Sci.-Pure Appl. Chem. 39 (2002) 643–656.
[12] J. Zhou, Z. Yao, Y. Chen, D. Wei, Y. Wu, Thermomechanical analyses of phenolic foam reinforced with glass fiber mat, Mater. Des. 51 (2013) 131–135.
[13] www.acelltec.com (accessed 12.01.15).
[14] J.F. Labuz, J.M. Bridell, Reducing frictional constraint in compression testing through lubrication, Int. J. Rock Mech. Min. Sci. Geomech. 30 (1993) 451–455.
[15] C. Gontier, A. Bouchou, C. Vinot, A mechanical model for the computation of phenolic foams in compression, Int. J. Mech. Sci. 43 (2001) 2371–2384.
[16] D.V. Ritzel, P.A. Thibault, Development of an efficient low-cost blast tube facility, in: Proc. Tenth Int. Symp. on Military Applications of Blast Simulation (MABS 10), Freiburg, Germany, 1987.
[17] D.V. Ritzel, et al. (Eds.), Nuclear Blast and Thermal Test Methods and Procedures, first ed., NATO Allied Engineering Publication, AEP-25, 1995.
[18] M. Colombo, P. Martinelli, M. di Prisco, Layered high performance concrete plates interacting with granular soil under blast loads: an experimental investigation, Eur. J. Environ. Civ. Eng. 17 (2013) 1002–1025.
[19] M. Colombo, P. Martinelli, M. di Prisco, On the blast resistance of high performance tunnel segments, Mater. Struct. (2015), http://dx.doi.org/10.1617/s11527-014-0480-7.
[20] M. Colombo, M. di Prisco, P. Martinelli, A new shock tube facility for tunnel safety, Exp. Mech. 51 (2011) 1143–1154.
[21] E.W. Andrews, G. Gioux, P. Onck, L.J. Gibson, Size effects in ductile cellular solids. Part II: Experimental results, Int. J. Mech. Sci. 43 (2001) 701–713.
[22] ABAQUS Analysis User's Manual, Version 6.12, vol. 2, 2012.
[23] V.S. Deshpande, N.A. Fleck, Isotropic constitutive model for metallic foams, J. Mech. Phys. Solids 48 (2000) 1253–1283.
[24] W. Chen, H. Hao, D. Hughes, Y. Shi, J. Cui, Z.-X. Li, Static and dynamic mechanical properties of expanded polystyrene, Mater. Des. 69 (2015) 170–180.
[25] Q.H. Shah, A. Topa, Modeling large deformation and failure of expanded polystyrene crushable foam using LS–DYNA, Model. Simul. Eng. (2014) 292–647.
[26] L. Di Landro, G. Sala, D. Olivieri, Deformation mechanisms and energy absorption of polystyrene foams for protective helmets, Polym. Test. 21 (2002) 217–228.
[27] J. Zhou, Z.W. Guan, W.J. Cantwell, Y. Liao, The energy-absorbing behaviour of foam cores reinforced with composite rods, Compos. Struct. 116 (2014) 346–356.
[28] M.C. Saha, H. Mahfuz, U.K. Chakravarty, M. Uddin, Md.E. Kabir, S. Jeelani, Effect of density, microstructure, and strain rate on compression behavior of polymeric foams, Mater. Sci. Eng. A 406 (2005) 328–336.